of the measured nonlinearity of the current in the junction to adjust the theoretical noise curve. This effect increases with bias voltage and so becomes more important at higher temperatures. Systematic effects at the lowest temperatures include nonlinearities in the conductance because of Coulomb blockade effects (*36*) and the frequency dependence of the noise at temperatures for which hf is comparable to $k_B T$, where f is the measurement frequency and h is Planck's constant. This quantum correction to the noise was observed (*37*) in a mesoscopic gold wire and can be easily corrected with a modification of the noise formula or eliminated by reducing the frequency of the measurement.

The above discussions address the precision of the SNT, but not the accuracy. To achieve the 1 to 100 ppm accuracy required to be of metrological interest, the linearity of the rf chain, the accuracy of the bias voltage measurement, and the precision of the temperature must all be at that accuracy, and the deviations in the noise from our simple model must be accounted for to that accuracy. The linearity of the measurement can be addressed by use of a null-balancing noise measurement as mentioned above, and part-per-million voltage accuracy can be achieved by using a well-calibrated nanovoltmeter. The nonlinearities in the noise from the junction should be correctable with the use of the measured voltage dependence of the conductance. If the accuracy can be brought down to the part-per-million level at the triple point of water, it may be possible to determine Boltzmann's constant directly (*38*). Even a 10 ppm accuracy measurement admits the possibility of determining the thermodynamic uncertainty of the low end of ITS-90 (*40*) and the high end of PLTS-2000 to competitive accuracy. Because the SNT has the desirable properties of being fast, compact, easy to use, and accurate over a wide range, it may have a much broader field of application than present primary thermometers.

References and Notes
1. R. L. Rusby *et al.*, *Metrologia* **33**, 409 (1996).
2. M. R. Moldover *et al.*, *Phys. Rev. Lett.* **60**, 249 (1988).
3. H. L. Callendar, *Philos. Mag.* **48**, 519 (1899).
4. B. N. Taylor, T. J. Witt, *Metrologia* **26**, 47 (1989).
5. J. P. Pekola, K. P. Hirvi, J. P. Kauppinen, M. A. Paalanen, *Phys. Rev. Lett.* **73**, 2903 (1994).
6. J. P. Kauppinen, K. T. Loberg, A. J. Manninen, J. P. Pekola, *Rev. Sci. Instr.* **69**, 4166 (1998).
7. P. Delsing *et al.*, *Physica B* **194**, 27 (1994).
8. A. J. Manninen *et al.*, *Physica B* **284–288**, 2010 (2000).
9. J. P. Pekola *et al.*, *J. Low Temp. Phys.* **128**, 263 (2002).
10. D. R. White, *Metrologia* **33**, 325 (1996).
11. J. B. Johnson, *Nature* **119**, 50 (1927).
12. J. B. Johnson, *Phys. Rev.* **32**, 97 (1928).
13. H. Nyquist, *Phys. Rev.* **32**, 110 (1928).
14. D. R. White, E. Zimmermann, *Metrologia* **37**, 11 (2000).
15. R. H. Dicke, *Rev. Sci. Instrum.* **17**, 268 (1946).
16. R. A. Webb, R. P. Giffard, J. C. Wheatley, *J. Low Temp. Phys.* **13**, 383 (1973).
17. C. P. Lusher *et al.*, *Meas. Sci. Technol.* **12**, 1 (2001).
18. R. A. Kamper, J. E. Zimmerman *J. Appl. Phys.* **42**, 132 (1971).
19. R. J. Soulen Jr., W. E. Fogle, J. J. Colwell, *J. Low Temp. Phys.* **94**, 385 (1994).
20. S. P. Benz, J. M. Martinis, S. W. Nam, W. L. Tew, D. R. White, in the Proceedings of Tempmeko 2001 (www.cstl.nist.gov/div836/836.05/papers/Tempmeko_01_JNT.pdf).
21. W. Schottky, *Ann. Phys.* **57**, 541 (1918).
22. T. Van Duzer, C. W. Turner, *Principles of Superconductive Devices and Circuits* (Elsevier North Holland, New York, 1981), pp. 75–78.
23. R. A. Pucel, *Proc. IRE* **49**, 1080 (correspondence) (1961).
24. A. J. Dahm *et al.*, *Phys. Rev. Lett.* **22**, 1416 (1969).
25. D. Rogovin, D. J. Scalpino, *Ann. Phys.* **86**, 1 (1974).
26. H. B. Callen, T. A. Welton, *Phys. Rev.* **83**, 34 (1951).
27. For example, even in a diffusive metal wire where the shot noise has the sub-Poisson value $S_1 = 2eI/3$ (*37*), the temperature extracted is the same.
28. J. Niemeyer, *PTB-Mitt.* **84**, 251 (1974).
29. G. J. Dolan, *Appl. Phys. Lett.* **31**, 337 (1977).
30. S. K. Tolpygo *et al.*, *IEEE Trans. Appl. Supercond.*, in press.
31. We used a rhodium-iron resistance thermometer (RF800-4-1.4L, Lakeshore Cryotronics, Westerville, OH, www.lakeshore.com) and a ruthenium-oxide resistance thermometer (RX202A-AA, Lakeshore Cryotronics).
32. J. P. Kauppinen, J. Pekola, *Phys. Rev. B* **54**, R8353 (1996).
33. L. Page, D. Wilkinson, *Rev. Mod. Phys.* **71**, S173 (1999).
34. J. D. Kraus *Radio Astronomy* (Cygnus-Quasar Books, Powell, OH, 1986), pp. 7–16.
35. At low temperatures, we assume diffusion cooling and use the Wiedemann-Franz law to compute the heating due to the finite lead resistance. Because the thermal conductance is proportional to temperature and the maximum power dissipated scales with temperature squared, the fractional temperature error is constant with temperature.
36. J. P. Kauppinen, J. P. Pekola, *Phys. Rev. Lett.* **77**, 3889 (1996).
37. R. J. Schoelkopf *et al.*, *Phys. Rev. Lett.* **78**, 3370 (1997).
38. P. J. Mohr, B. N. Taylor, *J. Phys. Chem. Ref. Data* **28**, 1713 (1999).
39. H. Preston-Thomas, *Metrologia* **27**, 3 (1990).
40. ITS-90 is the international temperature scale of 1990 and PLTS-2000 is the provisional low-temperature scale of 2000.
41. We thank M. Devoret, B. Jarvis, K. Likharev, D. Prober, and W. Tew for useful discussions and the David and Lucile Packard Foundation for support.

Oscillatory Thermomechanical Instability of an Ultrathin Catalyst

Fehmi Cirak,[1] Jaime E. Cisternas,[2] Alberto M. Cuitiño,[5] Gerhard Ertl,[6] Philip Holmes,[2,3] Ioannis G. Kevrekidis,[4,2] Michael Ortiz,[1] Harm Hinrich Rotermund,[6]* Michael Schunack,[6] Janpeter Wolff[6]

Because of the small thermal capacity of ultrathin (~200 nanometers) metal single crystals, it is possible to explore the coupling of catalytic and thermal action at low pressures. We analyzed a chemothermomechanical instability in this regime, in which catalytic reaction kinetics interact with heat transfer and mechanical buckling to create oscillations. These interacting components are separated and explored through experimentation, mathematical modeling, and scientific computation, and an explanation of the phenomenon emerges from their synthesis.

Pattern formation during a surface reaction can be critically affected by temperature changes that are caused by the heat of reaction. Changes in surface temperature locally alter the kinetics of the fundamental processes involved and might lead to ignition and traveling fronts on the active catalyst. Experimental studies of these processes often require tradeoffs: higher gas pressures lead to larger total heat production but also limit the use of surface-sensitive methods for observing fundamental processes.

One way to avoid this tradeoff is to work with ultrathin substrates that have much lower thermal inertia, such as those that have been pioneered by King and co-workers in microcalorimetry studies of surface reactions (*1*). To study pattern formation during the oxidation of CO on a platinum surface beyond the low-pressure, essentially isothermal regime (*2*), we used ultrathin (200-nm-thick) Pt(110) single crystals, which should be able to exhibit intense nonisothermal effects for this reaction at intermediate pressures (10^{-2} mbar) (Fig. 1A).

Photoemission electron microscopy (PEEM) images at 4×10^{-4} mbar revealed "raindrop" patterns on the sample, similar to those found before at much higher pressure on a bulk crystal (*3*), and substantiated their nonisothermal origin. At 5×10^{-3} mbar, where PEEM is not operable, we used a sensitive infrared camera (*4*), whose main component is a cooled InSb array, capable of imaging temperature differences of

---
[1]Division of Engineering and Applied Science, California Institute of Technology, Pasadena, CA 91125, USA. [2]Program in Applied and Computational Mathematics, [3]Department of Mechanical and Aerospace Engineering, [4]Department of Chemical Engineering, Princeton University, Princeton, NJ 08544, USA. [5]Department of Mechanical and Aerospace Engineering, Rutgers University, Piscataway, NJ 08854, USA. [6]Fritz-Haber-Institut der Max-Planck-Gesellschaft, Faradayweg 4-6, 14195 Berlin, Germany.

*To whom correspondence should be addressed. E-mail: rotermun@fhi-berlin.mpg.de

25 mK at room temperature. Strong temperature variations of up to 30 K from the working temperature of about 530 K were found, but, unexpectedly, the entire surface appeared to buckle. A simple check with a charge-coupled device camera using diffuse illumination from an ion gauge revealed intense crags, indicating that the heat of reaction raised the temperature of the single-crystal catalyst enough to result in substantial thermal expansion and thermoelastic buckling. However, at constant parameter settings, the buckled surface returned to its original flattened state and oscillated between these two appearances with a characteristic frequency (Fig. 1B) (*4*, *5*). Here, we present a systematic experimental and theoretical exploration of this chemothermomechanical phenomenon, which is represented by Scheme 1. The oscillation period of ~5 s is characterized by the repeated appearance of elongated ridges; the temperature rise during the buckled state is estimated to be about 20 K. Depending on conditions, this chemothermomechanical oscillation period ranges from 0.5 to 10 s. Temperature rises up to 30 K at 5×10^{-3} mbar O_2 partial pressure were measured, and the surface buckling intensity varied from the intense (tens of micrometers) crags of Fig. 1C (movie S1) to small (micrometer-sized) ridges.

In the experiments, chemical kinetics, thermochemistry, and heat transport, as well as large deformation (nonlinear) elastodynamics, are strongly coupled. We attempted to isolate each element and two-way interaction and to evaluate their roles in the chemical, temperature, and strain fields separately, in an effort to understand the complicated interactions as an integrated system. Our final synthesis is based on the results of judicious modeling simplifications, complementary experiments, and computations.

We decoupled thermoelastic buckling of thin plates under external heat sources from the heat of reaction by locally heating the crystal with a mildly focused (millimeter-sized) laser beam. (Fig. 2, A and B). Under equilibrium ultrahigh vacuum conditions at room temperature with reactants absent, and heating only the central region, numerous small-amplitude ridges appeared at 100- to 150-mW power (Fig. 2A); a 600-mW beam caused substantial deformation with fewer, larger folds or crags (Fig. 2B). These experiments and temperature-field observations under reaction conditions show that crystal center–support temperature differentials of a few degrees kelvin are typically needed for buckling to be observed. Rotation of the substrate (movie S2) also turned the ridges, suggesting that deformations are determined by anisotropy of the catalyst and/or support, and not by asymmetry of the laser beam or background radiant heat source.

At an elevated temperature (487 K), with only one reaction gas present, 100-mW laser power did not produce visible crystal deformation. The radiative heat loss, dominating at higher temperatures, sufficiently limits the temperature rise. Rapidly exchanging the reactant gases resulted in one reactive transition, and a transient set of ripples (Fig. 2C) appeared, similar to those of Fig. 2A. Switching the gas phase from O_2 to CO resulted in a fast surface-coverage swap (≤1 s) (movie S3). The reverse surface-coverage shift, from CO molecules to O atoms, is slower (~6 s). The difference in time scales for the two exchange reactions is caused by the asymmetric adsorption properties of the two reactants: CO covers the surface completely, inhibiting any immediate reaction, whereas the O atom coverage always remains "porous," allowing the switchover to proceed much faster. The reactive titration of just a single monolayer of one reactant by the other during the switch leads to macroscopic mechanical deformations.
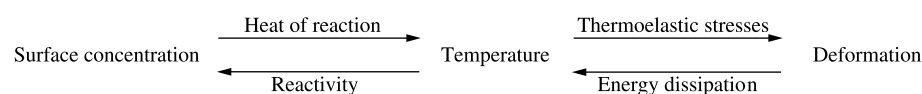
To model thermal and heat transport effects, we supplemented the isothermal chemistry model of (*6*) with the following heat balance equation, which includes conduction and radiation along with thermochemistry as heat sources and sinks

$$hc_p\rho \frac{\partial T}{\partial t} = \overbrace{h\kappa_{cond}\nabla^2 T}^{\text{conduction}} - \overbrace{\varepsilon\sigma(T^4 - T_{env}^4)}^{\text{radiation}}$$
$$+ \underbrace{\dot{q}_{chem}}_{\text{thermochemistry}} + \underbrace{\dot{q}}_{\text{other sources}}$$

(1)

where h is the thickness of the Pt plate; c_p is the heat capacity of the Pt; ρ is the density of the Pt; κ_{cond} is the thermal conductivity of the Pt; ε is the emissivity of the plate; σ is the Stefan-Boltzmann constant; T is the temperature of the plate; T_{env} is the temperature of the environment (reaction chamber), here room temperature; $\dot{q}$ is the rate of heat input resulting from nonchemical sources; and $\dot{q}_{chem}$ is the rate of heat input resulting from chemical sources. Chemical- and heat-diffusion time-scale computations (*7*) show that, for the experimental conditions, we can assume instantaneous thermal equilibration of the catalyst, but the radiation and conduction to the boundary cause nonuniform spatial temperature fields (Fig. 2I). Moreover, chemistry and heat transport are mutually coupled by means of the source terms in Eq. 1 and the Arrhenius temperature dependence of the desorption rate (k_{des}), the reaction rate (k_r), and the phase transition rate (k_{ph}) of the reaction diffusion equations in (*6*), which are detailed in (*7*) and summarized in the supporting material (*4*). The relatively massive substrate effectively provides fixed temperature-boundary conditions for the thin catalyst plate. [Fig. 3A shows a representative bifurcation diagram of this thermochemistry subsystem with respect to support temperature (T_{sup}).] The radiation term in Eq. 1 encompasses heat transfer from both sides of the plate and includes incident heat from the halogen lamp below the sample.

Oscillations appear in the appropriate frequency range, in which the varying catalyst temperature is effectively slaved to the chemistry. We have been able to combine Eq. 1 with equations describing the reaction-diffusion processes and the Pt(110) surface reconstruction [see supporting online materi-
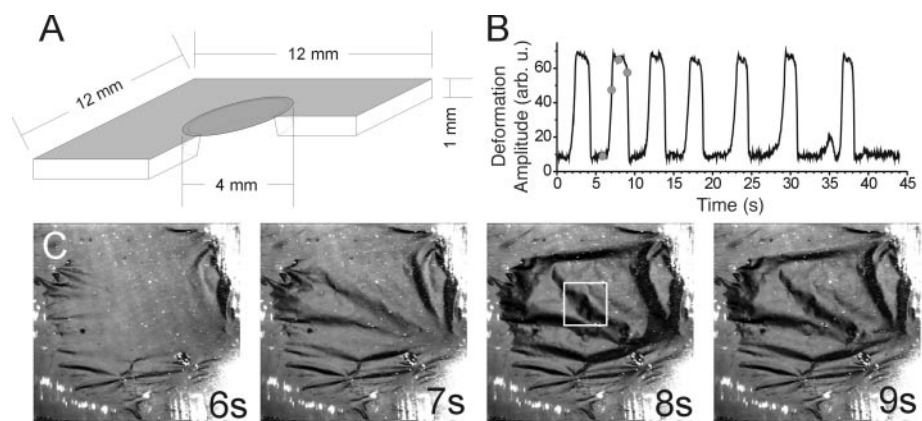
Heat of reaction →

Surface concentration ⇌ Temperature

← Reactivity

Thermoelastic stresses →

Temperature ⇌ Deformation

← Energy dissipation

Scheme 1.

Fig. 1. (A) The catalyst and substrate geometry. **(B)** Deformation oscillations of the catalyst as time progresses, measured by integrating the gray-scale values within the square of 100 × 100 pixels shown in the third frame of (C). arb. u., arbitrary units. **(C)** Diffuse light images from movie S1 of the catalyst surface deformations for a half-period at selected instants, as indicated by the four dots in (B). Images are 4.4 mm square.

al (SOM) text] to a four-dimensional (4D), lumped model of ordinary differential equations capable of capturing the salient features of the thermo-chemical oscillations (7). The temperature field, thus generated on the catalyst, causes thermoelastic buckling.

Experimental observations, whether with reaction- or laser-induced heating, revealed negligible acoustic ringing; kinetic energy was rapidly dissipated. We may therefore neglect dynamic effects and use the equilibrium equations of elastostatics, effectively implying that the crystal instantaneously assumes a (local) energy minimum in response to thermal stresses. Because the crystal is extremely thin, the deformations are preferentially accommodated through bending rather than stretching. Heat generated by mechanical stretching and compression may thus be neglected, removing the elastic deformation-temperature link of our interaction scheme. Neglecting back-coupling from the catalyst stress and deformation fields to the chemistry leads to a conceptual simplification: Thermochemistry interacts unidirectionally with thermomechanics, effectively by specifying heat sources to which the temperature field is slaved. In turn, elastostatic stresses are slaved to the temperature field. We can therefore entirely separate the temperature and elastic deformation components in our interaction scheme and study the thermoelastic problem with surrogate heat sources.

For both given temperature fields and fields derived by solution of the heat equation with fixed sources and conductive and radiative losses, we computed bifurcating families of elastic equilibria. We formulated a generalized von Kármán model, including in-plane (thermally induced, extensional) and out-of-plane (bending) deformations (8, 9). We used linear constitutive (stress-strain) relations, and because temperature ranges are relatively modest, neglected softening effects in the elastic moduli. Clamped boundary conditions are applied to model the effect of bonding to a massive, essentially rigid substrate at the perimeter of the hole (Fig. 1A). Only leading-order nonlinear terms were included in this asymptotic theory, which has the advantage that analytical results may be derived and used to check numerical solutions. Because the aspect ratio of the crystal is so small and the problem is singularly perturbed, with bending and extensional energies in the ratio (thickness/diameter)^2, such checks are important.

To obtain a detailed description of the deformation evolution of the crystal, fully nonlinear elastic equilibria must be sought. Furthermore, Fig. 1C suggests that debonding and boundary imperfections may play a role, so we need to allow for complex geometry. We computed such states by applying finite element simulations (SOM text) on unstructured meshes (Fig. 2D), using a Kirchhoff-Love thin-shell kinematic assumption that permits arbitrarily large displacements and rotations. The resulting strain energy is an asymptotic limit of the full 3D energy as the thickness/diameter ratio approaches zero (10), and because it depends on first- and second-order derivatives of displacement, the shape functions should exhibit slope continuity across element boundaries. We therefore adopted nonlocal smooth subdivision shape functions that interpolate displacements within each finite element by using its own vertices and its immediately adjacent vertices (11, 12), yielding a discrete minimization problem that typically has multiple local solutions (13, 14). A dynamic relaxation method was used to find equilibria corresponding to long-term limits of damped dynamic states.

Fig. 2. [(A) to (C)] Diffuse light images of catalyst surface deformation under (**A**) weak-laser and (**B**) strong-laser spot excitation in the absence of reactive gases, and (**C**) after rapid exchange of the reactive components. (**D**) The unstructured finite element grid for a plate with an imperfect boundary. (**E**) The first bifurcating mode of the von Kármán plate model. [(F) to (H)] Large-amplitude deformed states of the fully nonlinear Kirchhoff-Love plate model under a uniform temperature field exceeding the support temperature by 75 K, for (**F**) an isotropic plate, (**G**) an anisotropic cubic-crystal plate, and (**H**) an isotropic plate with imperfect boundaries. (**I**) Temperature distribution of the sample without reaction and averaged for 60 s. Infrared images at the trough in the thermal oscillation cycle (fig. S1) display a similar distribution. [(J) and (K)] Large-amplitude deformed states of the fully nonlinear Kirchhoff-Love plate model under nonuniform temperature fields exceeding the support temperature by (**J**) 7.5 K and (**K**) 75 K at the center, for the isotropic plate with an imperfect boundary subject to anisotropic (uniaxial) tensile prestrain of 0.0004; pronounced oriented ridges are seen. Out-of-plane deformations are multiplied by a factor of 2 in [(F) to (H)] and by a factor of 5 in [(J) and (K)]. (**L**
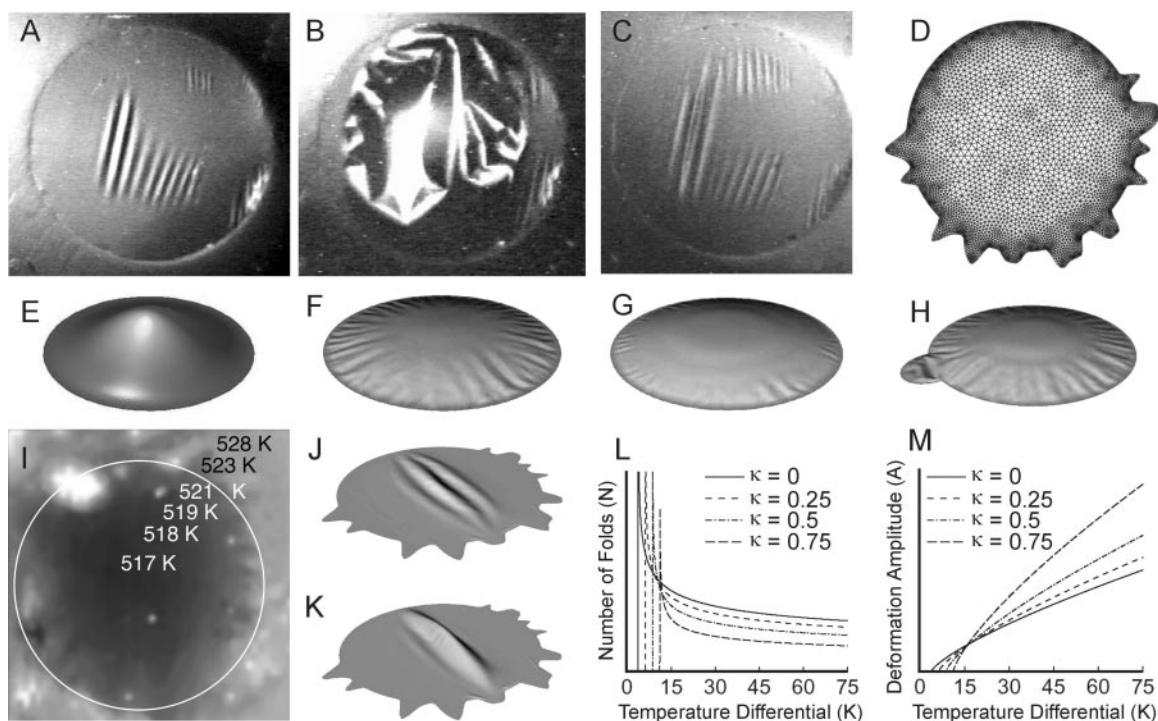
and **M**) Scaling arguments give the variation of the number of ridges and corresponding amplitudes with temperature differential and initial prestrain anisotropy κ (κ = 0 denotes uniaxial pretension, κ = 1 denotes isotropic tension). The number of ridges decreases and their amplitudes increase as the temperature differential rises, in accordance with the experiment. The vertical lines in (L) correspond to the critical temperature where the instability from a flat to a wavy film is triggered. At the critical point, the number of folds becomes unbounded but the corresponding amplitudes are zero. The critical temperature is proportional to the initial tensile prestrain and inversely proportional to the thermal expansion coefficient.

For small support-plate temperature differentials, these computations confirm the von Kármán bifurcation results above. In particular, they verified that even a very small temperature rise of O (10^{-4} K), which is well below the experimentally observed values, can cause primary buckling in the simulations as a result of the small thickness/diameter ratio. As temperature fields become more intense, substantial nonlinear buckling emerges, but large amplitudes, boundary imperfections, and the inclusion of mild (10%) crystal anisotropy (Fig. 2, F to H) cannot by themselves produce the oriented ridges and crags shown in Fig. 1C and Fig. 2, A and B.

Reexamining the data, we observed that the near-axisymmetric temperature distribution before heating exhibited lower values at
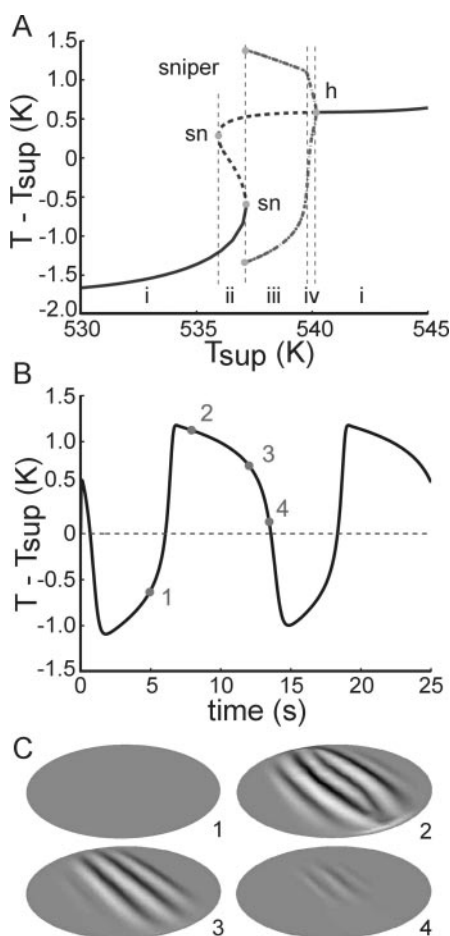

Fig. 3. (**A**) A bifurcation diagram showing branches of steady and periodic solutions of the model equations (*4*) as the substrate temperature varies. The oscillations of interest occur in the region marked (iii) [adapted from (*7*)]. (**B**) Temperature-time series from our model equations in region (iii). (**C**) Surface deformations for the fully nonlinear Kirchhoff-Love model at the instants marked 1 to 4 in (B). The oriented ridges intensify and decay as the temperature waxes and wanes, and the plate is in tension during the part of the cycle with $T - T_{sup} < 0$ (circle 1).

the center, as seen in Fig. 2I (central portions preferentially radiate heat, without low mean-free-path gas molecules which, at higher pressures, equalize the temperature). Thus, after placement in the chamber, tensile prestrains developed upon the establishment of a vacuum, as is visually corroborated by the "stretched membrane" wrinkles of Fig. 1C before and after buckling. Moreover, anisotropy of the prestrained state is corroborated by the elliptical shape of a hole that was inadvertently pierced in the crystal by an intense laser beam.

This anisotropic prestraining accounts for the deformation patterns, as shown in Fig. 2, J and K. Tensile prestrains stabilized the plate against thermal expansion, leading to the relatively large temperature differentials needed to produce buckling, in place of O (10^{-4} K) differentials in the absence of prestrain. Prestrain anisotropy changed buckling patterns from global modes (compare with Fig. 2, E to H) to ridges (*15*) and selected their orientation. Fewer and larger ridges emerged as the temperature differential increased (Fig. 2, J and K). As increasing thermal stresses were superimposed on the initial anisotropic tensile state, it first evolved to a highly anisotropic compressive state and then became less anisotropic as the temperature continued to rise. This reduction of compressive anisotropy with increasing temperature can be related to a reduction of the number of ridges and an increase in their magnitudes, in agreement with the experiments shown in Fig. 2, A and B.

Scaling laws (SOM text and fig. S2) for the number of ridges, *N*, and out-of-plane deformation amplitude, *A*, were obtained by minimizing the stretching and bending energy given by the von Kármán plate theory in the thin-plate (zero-thickness) limit. We obtained the preferred folding pattern by first finding states that minimize the stretching energy and then selecting those patterns that display the smallest ridge length (*15*). The theory predicts that *N* and *A* depend on the initial tensile anisotropy, κ, and temperature differential as shown in Fig. 2, L and M. These theoretical estimates show that (i) a critical temperature on the order of (maximum tensile prestrain)/(thermal expansivity) is required to induce buckling; (ii) after this temperature is exceeded, a relatively large number of small-amplitude folds appear; and (iii) with further temperature rises, the number of folds decreases and their amplitudes grow. As the initial degree of anisotropy was reduced (κ → 1), critical temperatures increased (Fig. 2M), but amplitudes also increased, and the number of folds was reduced (rightmost parts of Fig. 2, L and M).

Thus, the ridges observed in laser-heating experiments were successfully reproduced. Similarly, we used the time-dependent temperature field emerging from the kinetic os-

cillations in the appropriate parameter range of the model equations (Eq. 1; SOM text, eqs. 1 and 2; Fig. 3A) as input to the quasisteady large deformation computations and correctly reproduced the chemothermomechanical oscillations of Fig. 1, B and C. Figure 3B shows a temperature-time series, illustrating that the plate goes through states of tension (center colder than support) and compression (center hotter than support), and Fig. 3C shows the (large- amplitude) buckled states, and a tensile state, corresponding to the time instants indicated.

All components of the synthesis so far are well integrated and are corroborated by modeling and new experimentation. Reaction causes heating, which in turn affects reaction rates, and heating causes large-amplitude buckling. The thermochemical model produces qualitatively the correct frequencies: A kinetic surface ignition starts the oscillation cycle, raises the temperature, and buckles the plate. The concomitant adsorbate depletion and temperature-induced desorption, however, quench the reaction; radiative heat transfer then cools the plate, which unbuckles. Thermoelasticity appears—anticlimactically—to provide only a visual sensor of the thermochemical oscillations.

Is the problem solved? We believe that, to the first approximation, the above analysis is correct: Chemistry and heat mutually interact, and heat drives mechanics. But mechanics, in turn, deform the catalyst surface. Smooth curved surfaces have different adsorption properties (*16*), and contemporary ab initio computational chemistry shows changes in the adsorbate energetics of crystals under stress (*17*, *18*).

In the original lumped model studies one further time scale, corresponding to faceting of the crystal, was necessary to produce the mixed-mode chaotic dynamics observed in certain regimes (*6*). It is suggestive that our initial observation of instability involved a period two (small followed by large) buckling cycle. Variation of surface energetics under strain, and the resulting modification of kinetics, may be necessary to reproduce these more complex dynamics. Such further corrections to the theory presented here can be derived from microscopic (atomic-scale) observations and from ab initio computations of structural transformations under strain.

Because simple optical pointers or interferometers can detect microscopic deformations of catalytic foils, the present findings may lead to ultrasensitive measurement devices for reaction rates.

References and Notes
1. N. Al-Sarraf, J. T. Stuckless, D. A. King, *Nature* **360**, 243 (1992).
2. M. Eiswirth, M. Bär, H. H. Rotermund, *Physica D* **84**, 40 (1995).

3. H. H. Rotermund, G. Haas, R. U. Franz, R. M. Tromp, G. Ertl, *Science* **270**, 608 (1995).
4. Materials and methods are available as supporting material on *Science* Online.
5. The preliminary observation was briefly reported in a review paper on surface imaging: H. H. Rotermund, *Curr. Opin. Sol. Stat. Mater. Sci.* **3**, 354 (1998).
6. K. Krischer, M. Eiswirth, G. Ertl, *J. Chem. Phys.* **96**, 9161 (1992).
7. J. Cisternas, P. Holmes, I. G. Kevrekidis, X. Li, *J. Chem. Phys.* **118**, 3312 (2003).
8. J. Cisternas, P. Holmes, I. G. Kevrekidis, *Physica D* **177**, 71 (2003).
9. W. Nowacki, *Thermoelasticity* (Addison-Wesley, Reading, MA, 1962).
10. D. Morgenstern, *Arch. Ration. Mech. Anal.* **4**, 145 (1959).
11. F. Cirak, M. Ortiz, P. Schroeder, *Int. J. Numer. Methods Eng.* **47**, 2039 (2000).
12. F. Cirak, M. Ortiz, *Int. J. Numer. Methods Eng.* **51**, 813 (2001).
13. M. Ortiz, G. Gioia, *J. Mech. Phys. Solids* **43**, 531 (1994).
14. G. Gioia, M. Ortiz, *Adv. Appl. Mech.* **33**, 119 (1997)
15. G. Gioia, A. DeSimone, M. Ortiz, A. M. Cuitiño, *Proc. R. Soc. London Ser. A* **458**, 1223 (2002).
16. M. Gsell, P. Jakob, D. Menzel, *Science* **280**, 717 (1998).
17. M. Mavrikakis, B. Hammer, J. K. Norskov, *Phys. Rev. Lett.* **81**, 2819 (1998).
18. Y. Xu, M. Mavrikakis, *Surf. Sci.* **494**, 131 (2001).
19. Partially supported by NSF Division of Mathematical Sciences grant 98-03752 (J.E.C., P.H., and I.G.K.), by NSF grant CMS98-20823 (A.M.C.), and a Humboldt prize (I.G.K.).

Spin-Polarized Hydrogen Atoms from Molecular Photodissociation

**T. P. Rakitzis,[1,3]* P. C. Samartzis,[2,3] R. L. Toomes,[3]
T. N. Kitsopoulos,[2,3] Alex Brown,[4]† G. G. Balint-Kurti,[5]
O. S. Vasyutinskii,[6] J. A. Beswick[7]**

The production of spin-polarized hydrogen atoms from the photodissociation of hydrogen chloride with circularly polarized 193-nanometer light is inferred from the measurement of the complete angular momentum distributions of ground state Cl(^{2}P$_{3/2}$) and excited state Cl(^{2}P$_{1/2}$) cofragments by slice imaging. The experimentally measured and ab initio predicted $a_q^{(k)}(p)$ parameters, which describe the single-surface and multiple-surface-interference contributions to the angular momentum distributions, are in excellent agreement. For laser pulses longer than about 0.7 ns, the polarization of the electron and the proton are both 36%.

The ability to control the spin of electrons and nuclei is central to many fields of science. Spin-polarized hydrogen (SPH) atoms, and polarized atoms in general, are used to study spin-dependent effects in nuclear, atomic, molecular, and surface collisions (*1*, *2*). They are also used, when produced by an external magnetic field, in nuclear magnetic resonance (NMR) spectroscopy in wide-ranging applications to measure molecular structure and dynamics (*3*). SPH is usually produced by the experimentally difficult techniques of Stern-Gerlach spin separation (*1*) and spin-exchange optical pumping (*2*).

We show that SPH can be readily produced from the photolysis of a "simple" diatomic molecule, HCl, which enhances its

[1]Department of Physics, [2]Department of Chemistry, University of Crete, Heraklion-Crete, Greece. [3]Institute of Electronic Structure and Laser, Foundation for Research and Technology–Hellas, 71110 Heraklion-Crete, Greece. [4]Department of Chemistry and Cherry L. Emerson Center for Scientific Computation, Emory University, Atlanta, GA 30322, USA. [5]School of Chemistry, University of Bristol, Bristol BS8 1TS, UK. [6]Ioffe Physico-Technical Institute, Russian Academy of Sciences, 194021 St. Petersburg, Russia. [7]Laboratoire de Collisions, Agrégats de Réactivité, Institut de Recherche sur les Systèmes Atomiques et Moléculaires Complexes, Université Paul Sabetier, 31062 Toulouse, France.

*To whom correspondence should be addressed. E-mail: ptr@iesl.forth.gr
†Permanent address: Department of Chemistry, University of Alberta, Edmonton, Alberta, T6G 2G2, Canada.

potential range of use. Molecular photodissociation is often viewed as taking place on a single adiabatic electronic state, but, in general, it can proceed through several dissociative electronic states (*4*, *5*) (Fig. 1). More important, after direct excitation from the ground electronic state to one or more energetically accessible excited electronic states, nonadiabatic transitions between these states (and possibly other states not directly linked to the ground state) can occur as the molecule dissociates (*6*, *7*). Additionally, these multiple dissociative pathways can interfere with each other quantum-mechanically. Our understanding of dissociation dynamics, and of the way systems evolve on multiple electronic states, requires the accurate experimental measurement of a variety of observables, particularly angular momentum distributions (*5–8*), combined with high-level theoretical calculations that incorporate all of these effects. We compare theory and experiment for the photodissociation of HCl.

The photodissociation of a diatomic molecule AB yields, in general, open-shell photofragments A and B that possess electronic angular momenta J_A and J_B, respectively. These angular momenta can have a preferred orientation in space and are associated with anisotropic electron distributions about the atomic photofragments (unless J_A or J_B comprise electron spin only). Van Brunt and Zare first proposed a mechanism for photofrag-

ment electronic polarization (*8*). More recently, Siebbeles *et al.* (*9*) have shown that the spatial distributions of the photofragment angular momenta can be decomposed into distinct contributions from single potential energy surface (PES) dissociation and from the interference from dissociation through multiple PESs. The magnitudes of these distinct spatial contributions can be described by the various $a_q^{(k)}(p)$ parameters, in which a is the alignment parameter, the indices k and q refer to the spatial distribution, and (p) refers to the symmetry of the transition from the ground state to the dissociating states (*10–12*). Most important, the values of $a_q^{(k)}(p)$, measured as a function of the dissociation energy, give an extremely detailed picture of
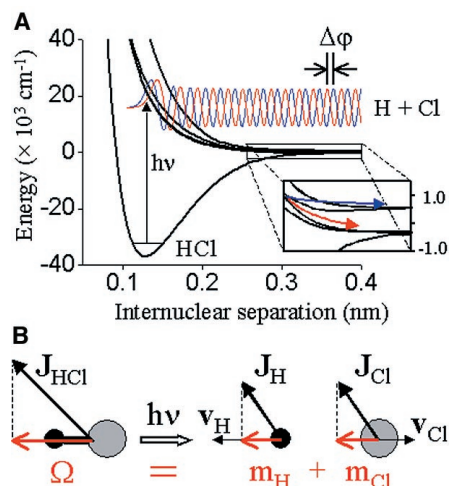

Fig. 1. (A) Plot of the ground state and four optically accessible, adiabatic potential energy curves of HCl used in the time-dependent wave-packet calculations, generated with information from (*15*), showing a phase shift ($\Delta\varphi$) generated in the wave functions of coherently excited states. hν is the energy of the absorbed photon. Inset: An expanded view of the long-range parts of the potentials (the two lowest excited states can now be resolved), showing nonadiabatic transitions from the $A^1\Pi_1$ state to the $a^3\Pi_1$ state (red arrow) and to the $t^3\Sigma_1$ state (blue) during dissociation; in order of increasing energy, the curves are $X^1\Sigma_{0+}$, $a^3\Pi_1$, $A^1\Pi_1$, $a^3\Pi_{0+}$, and $t^3\Sigma_1$. **(B)** The projection along the recoil direction of the electronic angular momentum of HCl is conserved between the projections of the angular momenta of H and Cl.